Editors' Suggestion

Probing defect states in few-layer MoS_2 by conductance fluctuation spectroscopy

Suman Sarkar and Aveek Bid*
Department of Physics, Indian Institute of Science, Bangalore 560012, India

K. Lakshmi Ganapathi
Department of Physics, Indian Institute of Technology, Madras 600036, India

Sangeneni Mohan
Centre for NanoScience and Engineering, Indian Institute of Science, Bangalore 560012, India

(Received 14 May 2019; revised manuscript received 11 June 2019; published 26 June 2019)

Despite the concerted effort of several research groups, a detailed experimental account of defect dynamics in high-quality single- and few-layer transition-metal dichalcogenides remains elusive. In this paper we report an experimental study of the temperature dependence of conductance and conductance fluctuations on few-layer MoS_2 exfoliated on hexagonal boron nitride and covered by a capping layer of high-κ dielectric HfO_2. The presence of the high-κ dielectric made the device extremely stable against environmental degradation as well as resistant to changes in device characteristics upon repeated thermal cycling, enabling us to obtain reproducible data on the same device over a timescale of more than 1 year. Our device architecture helped bring down the conductance fluctuations of the MoS_2 channel by orders of magnitude compared to previous reports. The extremely low noise levels in our devices made it possible to detect the generation-recombination noise arising from charge fluctuation between the sulfur-vacancy levels in the band gap and energy levels at the conductance band edge. Our work establishes conduction fluctuation spectroscopy as a viable route to quantitatively probe in-gap defect levels in low-dimensional semiconductors.

DOI: 10.1103/PhysRevB.99.245419

I. INTRODUCTION

Following the discovery of graphene [1], the exploration of the basic physics and technological implications of two-dimensional (2D) materials has gained tremendous importance. Although graphene is a system rich in novel physics, the lack of a band gap limits its applications in transistor technology. Transition-metal dichalcogenides (TMDs) like MoS_2 and $MoSe_2$, on the other hand, have band gaps of the order of eV in the few-layer limit [2], making them ideal for optoelectronic applications [3–5]. On the flip side, the reported mobilities of these TMD-based field-effect transistor (FET) devices are very low [6], and the quoted values vary widely between samples. It is now understood that defect levels (primarily arising from chalcogenide vacancies) adversely affect the mobility and optical properties of these TMD-based devices [7–10].

Despite extensive research, there is no clear understanding of the underlying defect dynamics in this system. Traditional transport measurements like current-voltage characteristics and the temperature dependence of the resistance, while providing indications of the existence of defect states, cannot directly probe their energetics [9,11]. Photoluminescence measurements report the appearance, at low temperatures, of an additional peak in the spectrum which is tentatively attributed to transitions from a "defect" level [12,13], but no direct evidence of this level has been found from optical studies. Transmission electron microscopy (TEM) [7,14–17] and scanning tunneling microscopy (STM) [18–23] have shown that the primary point defects are *S* vacancies, although other types of defects like interstitials, dislocations, dopants, and grain boundaries were also seen. These two techniques come with their own sets of limitations. While TEM imaging is believed to induce additional defects in MoS_2 [24,25], atomic-resolution imaging of few-layer TMDs using STM has proved challenging [11,26–28]. Thus, although theoretical studies predict the presence of prominent defect levels in these materials [29–33], probing them experimentally has proved to be challenging.

In this paper, we present conductance fluctuation spectroscopy [34] as a viable technique to identify these defect states and their characteristic energy levels. Conductance fluctuations (noise) in TMD-based devices has been studied by several groups [35–39]. In different studies, the observed conductance fluctuations have been variously attributed to charge-carrier number density fluctuations due to trapping at the interface [36], to mobility fluctuations [37,38], or to contact noise [39]. In general, in the high-doping regime, the carrier number density fluctuation model could explain the measured noise behavior, while in the low-doping regime mobility fluctuation models seemed to better fit the experimental observations [40]. Thus, there is a lack of consensus in the community as to the origin of the observed large conductance fluctuations in this system. The problem is aggravated by the fact that ultrathin layers of TMDs degrade extremely fast

*aveek@iisc.ac.in

when exposed to the ambient [39,41–43]. This makes repeated, reliable measurements on the same device challenging while at the same time severely limiting the scope of practical applications.

We have performed detailed measurements of the temperature T dependence of conductance and conductance fluctuations on several few-layer MoS_2 exfoliated on hexagonal boron nitride (hBN) and covered by a film of high-κ dielectric HfO_2. We find that over a large range of T, the noise in the system is dominated by generation-recombination processes caused by random charge fluctuations via transitions between the S-vacancy impurity band and the conduction band of MoS_2. The presence of the HfO_2 capping layer makes it extremely stable against degradation upon exposure to the atmosphere and to repeated thermal cycling. The presence of the crystalline hBN below screens the device from charge fluctuations in the SiO_2 substrate, resulting in the noise levels in our device being orders of magnitude smaller than previous reports of on-substrate devices. This enabled us to detect charge fluctuations between the S-vacancy levels and the conduction-band edge.

II. DEVICE FABRICATION AND MEASUREMENT DETAILS

Samples were prepared in the FET configuration by the conventional polydimethylsiloxane (PDMS)-assisted dry-transfer method [44]. We studied two classes of devices. In the first class, a few-layer hBN flake (≈20 nm thick) was transferred on a Si^{++}/SiO_2 substrate followed by the transfer of a few-layer MoS_2 on top. The transfers were made using a custom-built setup based on a motorized XYZ stage (Thorlabs model B51x) using a long-working-distance 50× objective under an optical microscope. Electrical contacts were defined by standard electron-beam lithography followed by thermal deposition of 5 nm of Cr and 25 nm of Au. This was followed by an electron-beam-assisted evaporation of 30 nm of HfO_2 covering the entire surface of the device. The HfO_2 thin film was deposited directly on MoS_2 without any buffer layer or surface treatment; the details of the HfO_2 film growth are discussed elsewhere [45,46]. Several such devices were tested. In this paper we concentrate on the results obtained on one such device, labeled D1. For comparison, we also studied a second class of devices; they were few-layer MoS_2 devices fabricated directly on the Si^{++}/SiO_2 substrate without the top encapsulation layer (labeled D2). The thickness of the SiO_2 in all cases was 295 nm. In all cases, the gate bias voltage V_g is applied from underneath the Si^{++}/SiO_2 substrate.

III. TEMPERATURE AND V_G DEPENDENCE OF RESISTANCE

Electrical transport measurements were performed in a two-probe configuration using a low-frequency lock-in technique. The bias voltage across the device was set to $V_{ds} =$ 5 mV. The current I_{ds} flowing through the device was amplified by a low-noise current amplifier (Ithaco 1211) and measured by a digital dual-channel lock-in amplifier (LIA). The gate voltage V_g was controlled by a Keithley-2400 source meter.

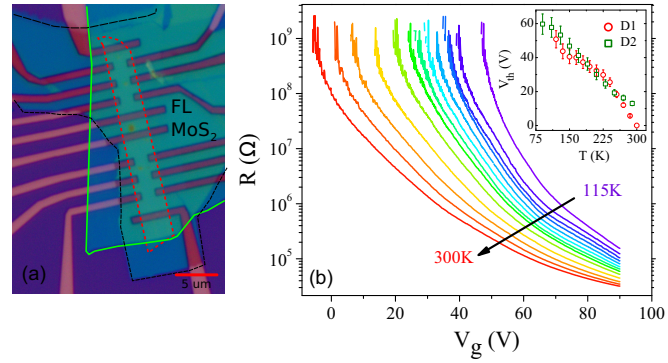

FIG. 1. (a) Optical image of device D1. The bottom, hBN, is defined with a solid green line and the few-layer (FL) MoS_2 is outlined by a red dashed line. The top, HfO_2, is outlined by a dashed black line. (b) Gate-voltage V_g dependence of the resistance R of device D1 at a few representative temperatures ranging from 115 to 300 K in steps of 15 K. The inset plots the onset voltage V_{th} versus T for devices D1 (red open circles) and D2 (green open squares).

An optical image of device D1 is shown in Fig. 1(a); the few-layer MoS_2 (encapsulated between hBN and HfO_2) is outlined by a black dashed line. Figure 1(b) shows a plot of the sheet resistance $R \equiv V_{ds}/I_{ds}$ of device D1 versus V_g measured over the temperature range 115–300 K. The gate response of the device establishes it to be an n-type semiconductor, which is typically what is observed in naturally occurring MoS_2. The large on-off ratio (∼10^5), low on-state resistance (∼30 KΩ), and very low off-state current (∼10 pA) attest to the high quality of the device. From the inset of Fig. 1(b) it can be seen that the threshold voltage V_{th} decreases sharply with increasing temperature going to negative V_g near room temperature. On the other hand, V_{th} for D2 at room temperature was ∼15 V.

In Fig. 2(a) we plot the sheet resistance R of device D1 in a semilogarithmic scale versus inverse temperature for a few representative values of V_g. The linearity of the plots indicates that, at least in the high-T limit, electrical transport is dominated by thermal activation of the charge carriers. More specifically, as we go higher in V_g, the range of T where this linearity holds extends down to lower temperatures. The activation energy ε extracted from the slope of the $\ln(R)$ versus $1/T$ plots is plotted in Fig. 2(b). One can see that ε increases as one decreases the gate bias, and it varies from 20 meV at high V_g to an order of magnitude higher, ∼200 meV, close to the off state of the device. The activation energy for device D2, extracted in a similar fashion, is, as expected, higher than that of D1 at all values of V_g.

The field-effect mobility μ of the devices can be obtained from the relation $\mu = \frac{dI_{ds}}{dV_g}\frac{L}{wCV_{ds}}$. Here L is the length of the channel, w is its width, and C is the gate capacitance per unit area. In Fig. 2(c) we show plots of I_{ds} versus V_g; the slope of this curve gives the mobility of the device. A plot of the T dependence of the mobility is shown in Fig. 2(d). We find that μ for device D1 is ∼20 $cm^{-2}\,V^{-1}\,s^{-1}$ at 100 K. With increasing T, μ increases monotonically until about 225 K, beyond which it begins to fall with increasing T. To understand the measured T dependence of μ we note that in 2D semiconductors, the mobility of the charge carriers is affected by Coulomb scattering, acoustic and optical phonon

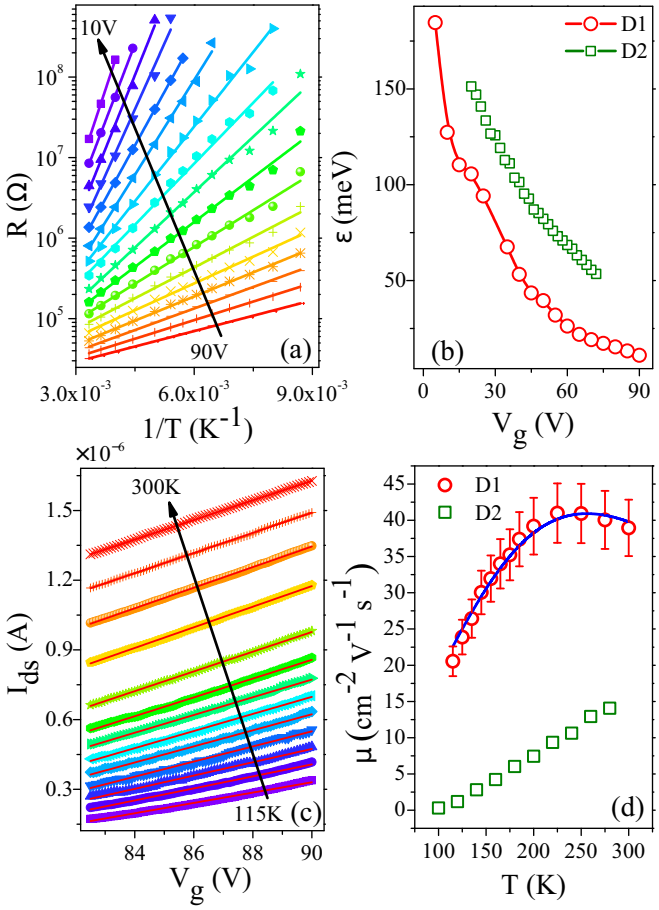

FIG. 2. (a) Scatterplot of resistance R of device D1 plotted on a semilogarithmic scale versus $1/T$ at several representative values of V_g from 10 to 90 V in steps of 5 V. The solid lines are the linear fits of $1/T$ vs $\ln(R)$. (b) Plots of activation energy ε versus V_g extracted from the $\ln(R)$ versus $1/T$ plots for the two devices, D1 (red open circles) and D2 (green open squares). The lines are guides to the eye. (c) Plots of I_{ds} versus V_g at different T ranging from 115 to 300 K for device D1. (d) Plots of mobility μ versus T for the two devices, D1 (red open circles) and D2 (green open squares). The blue line is a fit to the data for D1 using Eq. (1).

scattering, scattering by the interface phonon, and roughness due to the surface [47]. At high T, scattering due to phonons is dominant, which causes the mobility to have a $T^{-3/2}$ dependence [48,49]. On the other hand, scattering from charge impurities located randomly in the sample is the dominant factor limiting μ at low temperatures, causing the mobility to depend on temperature as $T^{3/2}$ [8,50]. Following Matthiessen's rule,

$$\frac{1}{\mu} = \frac{1}{M_p T^{-3/2}} + \frac{1}{M_i T^{3/2}}, \tag{1}$$

where M_p and M_i represent the relative contributions of the phonon-scattering and impurity-scattering mechanisms, respectively. These coefficients are not independent but are related by $(M_p/M_i)^{1/3} = T_{\max}$, where $T_{\max}$ is the temperature at which μ has a maximum. In Fig. 2(d) we show a fit of the T dependence of the mobility of D1 to Eq. (1). The mobility of D2, on the other hand, monotonically increases with T,

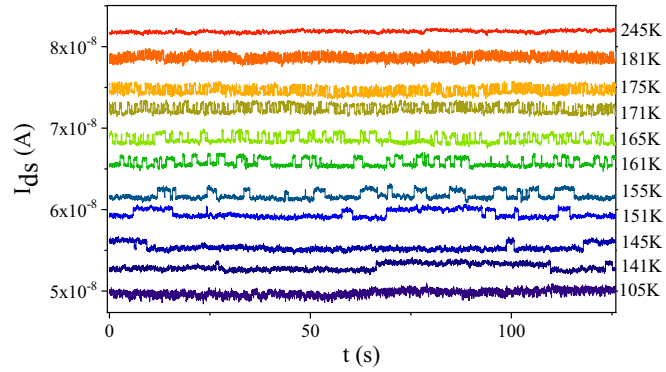

FIG. 3. Plots of source-drain current I_{ds} versus time at a few representative temperatures from 105 to 245 K for device D1. The data were taken for $V_g = 90$ V.

showing that over the range of T studied, impurity scattering dominates the transport in on-SiO_2 substrate devices.

IV. CONDUCTANCE FLUCTUATION SPECTROSCOPY

The presence of both bulk- and surface-transport channels complicates the charge transport in these systems. To understand the charge-carrier dynamics arising from the surface and bulk states in this system, we studied the low-frequency conductance fluctuations over the temperature range 70–300 K using a two-probe ac digital-signal-processing technique [51]. As established in several previous reports, $1/f$ noise is an excellent parameter to probe interband scattering of charge carriers in systems with multiple conduction channels [52–54]. We used an SR830 dual-channel digital LIA to voltage bias the sample at a carrier frequency of $f_0 \sim 228$ Hz. The current I_{ds} through the device was amplified by the low-noise current preamplifier and detected by the LIA. The data were acquired at every T and V_g for 32 min at a sampling rate of 2048 points/s using a fast 16-bit data acquisition card. This time series of current fluctuations $\delta I_{ds}(t)$ was digitally antialias filtered and decimated. The power spectral density (PSD) of current fluctuations $S_I(f)$ was calculated from this filtered time series using the method of the Welch periodogram [51,55]. The system was calibrated by measuring the thermal (Johnson-Nyquist) noise of standard resistors. The time series of I_{ds} measured for device D1 at a few representative temperatures at $V_g = 90$ V are shown in Fig. 3. We find that over the T range of ~140–190 K, the measured $I_{ds}(t)$ [and, consequently, the conductance $g(t) = I_{ds}(t)/V_{ds}$] for D1 fluctuates between two well-defined levels [56,57]. This "random telegraphic noise" (RTN) [58] usually signifies that the system has access to two (or more) different states separated by an energy barrier. We come back later in this paper to a discussion of the detailed statistics of the RTN and the physical origin of these states.

In Fig. 4(a) we plot the PSD of current fluctuations at a few representative values of T and $V_g = 90$ V for device D1. We find that over the T range where RTNs were present in the time series $I_{ds}(t)$, the PSD deviates significantly from the $1/f$ dependence (shown in the plot by a gray line). This can be appreciated better from Fig. 4(b), where we plot the quantity

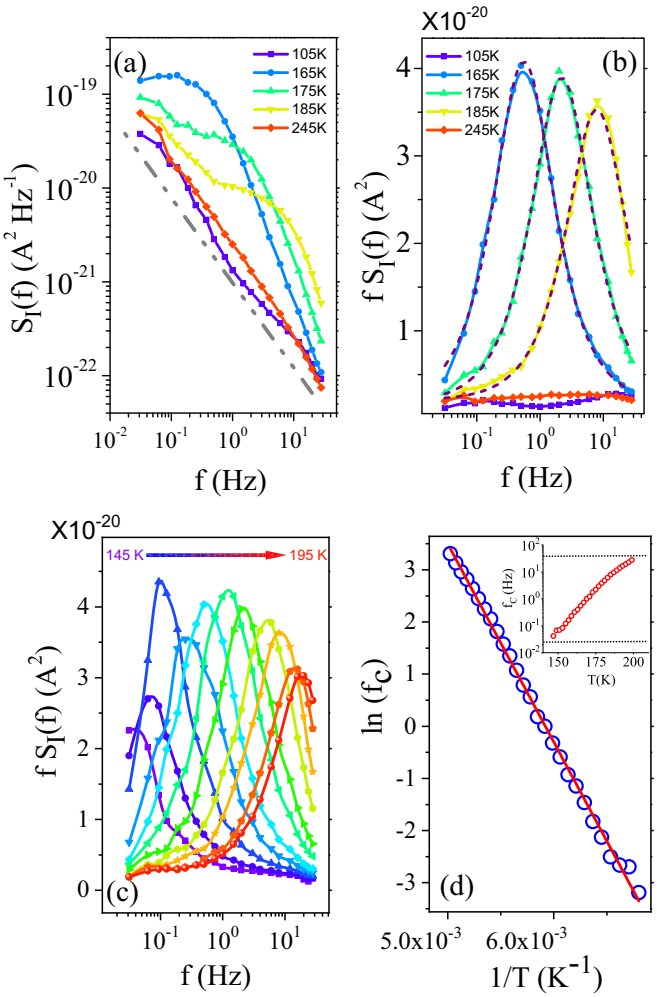

FIG. 4. (a) Plots of $S_I(f)$ versus f at a few representative temperatures for device D1. The data were measured for $V_g = 90$ V. (b) Plots of $fS_I(f)$ versus f for the same values of T as in (a). The dotted purple lines are fits using Eq. (2) to the data at 165, 175, and 185 K. (c) Plot of $fS_I(f)$ as a function of f over the temperature range from 145 K (purple data points) to 195 K (red data points) in steps of 5 K. The arrow indicates the evolution of f_C to higher values with increasing T. The solid lines are guides to the eye. (d) Plot of the logarithm of f_C versus $1/T$. The solid line is a linearized fit to the Arrhenius relation $f_C = f_0 \exp(-E_a/k_BT)$. The inset shows a plot of f_C versus T. The two dotted lines are the upper (28 Hz) and lower (31.25 mHz) limits of our measurement bandwidth.

$fS_I(f)$, which should be independent of frequency for the $1/f$ noise, as is indeed the case for the PSD measured at 105 and 245 K. On the other hand, the PSD measured in the intermediate T range (140 K $< T <$ 190 K) has a significant non-$1/f$ component. The PSD of an RTN is a Lorentzian with a characteristic frequency f_C, where $1/f_C = \tau_c$ is the typical timescale of switching between the two distinct levels. This motivated us to fit the measured PSD of current fluctuations to an equation which contains both $1/f$ and Lorentzian components:

$$\frac{S_I(f)}{I^2} = \frac{A_1}{f} + \frac{A_2 f_C}{f^2 + f_C^2}. \tag{2}$$

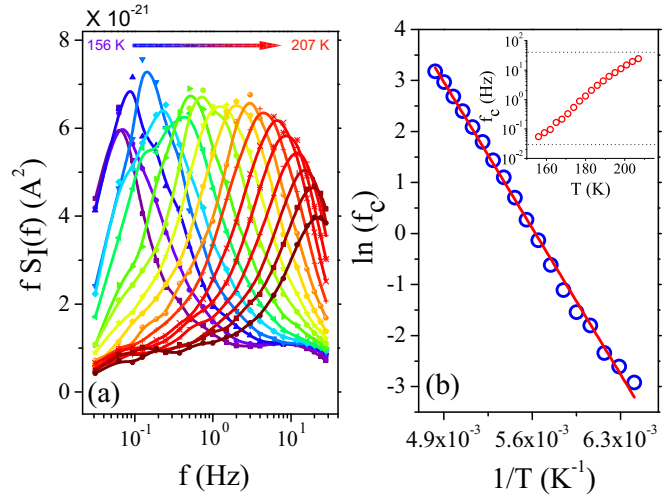

FIG. 5. (a) Plot of $fS_I(f)$ as a function of f over the temperature range from 156 K (purple data points) to 207 K (red data points) in steps of 4 K for device D1b. (b) Plot of the logarithm of f_C versus $1/T$. The solid line is a linearized fit to the Arrhenius relation $f_C = f_0 \exp(-E_a/k_BT)$. The inset shows a plot of f_C versus T. The measurements were done at $V_g = 90$ V.

A_1 and A_2 are fit parameters that denote the relative contributions of the random and RTN fluctuations, respectively, to the total PSD. The dotted purple lines are fits to the data at 165, 175, and 185 K using Eq. (2). In Fig. 4(c) we show plots of $fS_I(f)$ versus f over an extensive range of T. We find that as T increases, the peak position evolves from a few millihertz to a few tens of hertz [see the inset of Fig. 4(d)]. Beyond this T range, the value of f_C goes beyond our measurement frequency bandwidth (31.25 mHz to 28 Hz). The value of f_C is thermally activated and follows the Arrhenius relation: $f_C = f_0 \exp(-E_a/k_BT)$. Figure 4(d) shows a plot of $\ln(f_C)$ versus $1/T$; the red line is a fit to the activated behavior. The value of activation energy E_a extracted from the fit is 370 meV. These measurements were repeated on three such devices (MoS_2 encapsulated between hBN and HfO_2); we find that the activation energy scales in all of them lie in the range 370 ± 30 meV. In Fig. 5, we show data for another device, D1b, for which we obtain $E_a = 353$ meV. We come back to the physical implications of this energy scale later.

The time series $\delta I(t)$ for device D2, on the other hand, did not have a RTN component [Fig. 6(a)], and the PSD had a $1/f^\alpha$ (with $0.9 < \alpha < 1.1$) dependence on f over the entire T and V_g range studied [Fig. 6(b)]. The $I_{ds}(t)$ data were obtained for device D2 at 72 V. We have attempted to compare the data in the two sets of devices at similar values of number densities. Due to the presence of the hBN layer, the effective thickness of the dielectric layer in D1 was higher than that of D2, requiring a higher gate voltage for D1 than that for D2 to achieve a similar carrier number density. On the other hand, D1 had a lower threshold voltage than D2. Taking both these factors into account, we have estimated the V_g at which the induced number densities are similar for both D1 and D2. Thus, for D1, the data are presented for $V_g = 90$ V, while for device D2, the data are presented for $V_g = 72$ V.

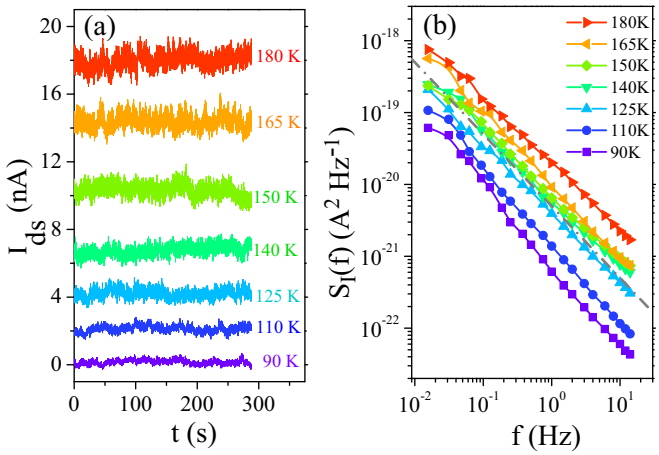

FIG. 6. (a) Plot of I_{ds} versus time at a few representative values of T for device D2. (b) PSD $S_I(f)$ corresponding to the time series shown in (a). The gray line shows a representative $1/f$ curve. The measurements were done at $V_g = 72$ V.

In Fig. 7(a) we present the V_{ds} dependence of the quantity $fS_I(f)$ measured at $T = 175$ K and $V_g = 90$ V for device D1. We see that the form of the PSD is independent of V_{ds}. To make this observation quantitative, we plot in Fig. 7(b) the dependence of f_C on V_{ds} extracted from these plots using Eq. (2). The fact that f_c is independent of V_{ds} within experimental uncertainties shows that this timescale is intrinsic to the sample [59].

The PSD $S_I(f)$ can be integrated over the frequency bandwidth of the measurement to obtain the relative variance of

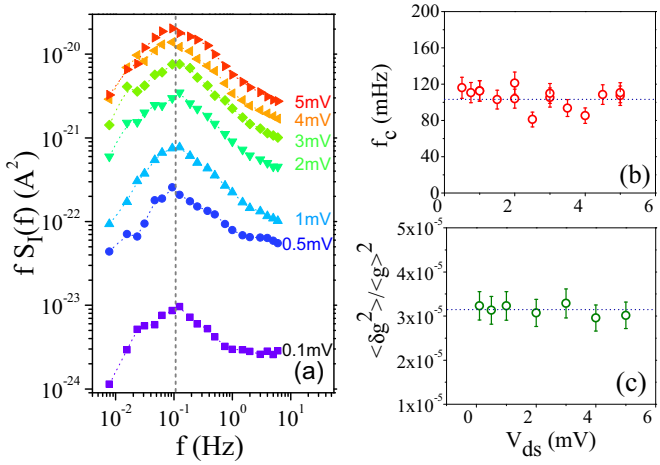

FIG. 7. (a) Plot of $fS_I(f)$ versus frequency f at different source-drain biases V_{ds} across sample D1. The vertical dashed gray line is a visual guide indicating the positions of the Lorentzian peaks in the spectra. The value of V_{ds} is marked next to each curve. (b). Plot of f_c as a function of V_{ds} extracted from the PSD in (a) using Eq. 2. The dotted line is a visual guide to the eye. (c) Plot of the relative variance of conductance fluctuations $\mathcal{G}_{\rm var}$ as a function of V_{ds}; the dotted line is a guide to the eye. The data were all taken at $T = 175$ K and $V_g = 90$ V.

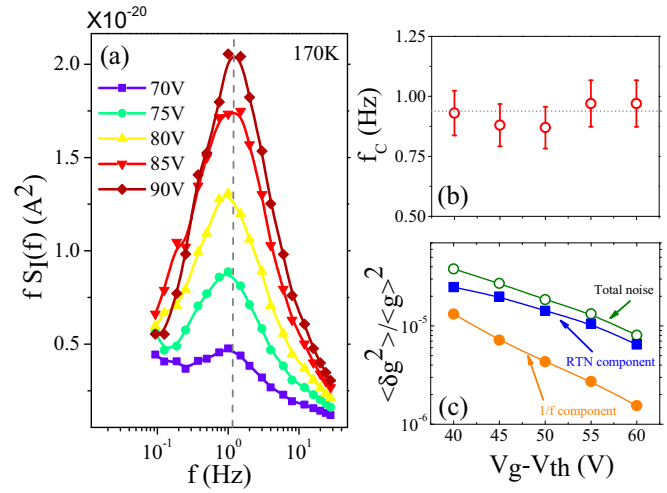

FIG. 8. (a) Plot of $fS_I(f)$ versus frequency f at different gate-bias voltages V_g across sample D1. The vertical gray dashed line is a visual guide indicating the positions of the Lorentzian peaks in the spectra. (b) Plot of f_c as a function of V_g-V_{th} extracted from the PSD in (a) using Eq. (2). The dotted line is a guide to the eye. (c) Plots of the relative variance of conductance fluctuations $\mathcal{G}_{\rm var}$, along with its RTN component and $1/f$ component versus V_g-V_{th}. The solid lines are guides to the eye. The data were all taken at $T = 170$ K and $V_{ds} = 5$ mV.

conductance fluctuations $\mathcal{G}_{\rm var}$ at fixed T and V_g:

$$\mathcal{G}_{\rm var} \equiv \frac{\langle \delta g^2 \rangle}{\langle g \rangle^2} = \frac{\langle \delta I_{ds}^2 \rangle}{\langle I_{ds} \rangle^2} = \frac{1}{\langle I_{ds} \rangle^2} \int_{0.03125}^{28} S_I(f) df. \qquad (3)$$

The relative variance of conductance fluctuations $\mathcal{G}_{\rm var}$ was found to be independent of V_{ds} at all T and V_g, confirming that the noise arises from conductance fluctuations in the MoS_2 channel and not from the contacts [for representative data, see Fig. 7(c)].

We measured the noise as a function of gate bias voltage V_g; the results obtained at $T = 170$ K for device D1 are plotted in Fig. 8(a). We find f_C to be independent of V_g [Fig. 8(b)] within experimental uncertainties. In Fig. 8(c) we plot $\mathcal{G}_{\rm var}$ as a function of V_g-V_{th}. The total noise has been separated into its $1/f$ component and the RTN component. At low values of V_g-V_{th}, the $1/f$-component noise contribution is comparable to that of the RTN component, while at higher V_g-V_{th}, the RTN component dominates the measured conductance fluctuations. This motivated us to perform our noise measurements at high V_g (90 V), so that the RTN component of the noise is easily resolvable.

In Fig. 9 we show a plot of $\mathcal{G}_{\rm var}$ versus T for the two devices. The noise data for device D1 (plotted by green open circles) has a prominent hump over the T range (∼140–190 K) coinciding with the regime where we observed RTN. To appreciate this, we plot on the same graph the relative variance of conductance fluctuations arising from the $1/f$ component (red solid circles) as well as the Lorentzian component (blue open circles). It can be seen that the increase in noise over the 140–190 K temperature range is entirely due to two-level conductance fluctuations in the system. For comparison, we also add a plot of $\mathcal{G}_{\rm var}$ versus T for the unencapsulated

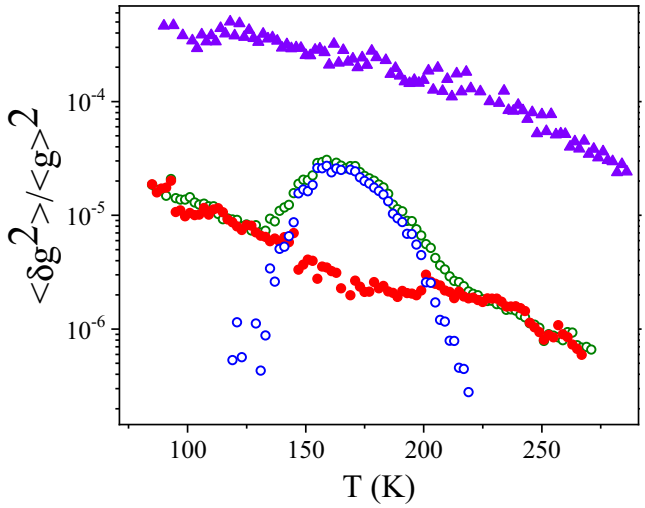

FIG. 9. Comparison of the measured relative variance of conductance fluctuations $\mathcal{G}_{\rm var} = \langle \delta g^2 \rangle / \langle g \rangle^2$ versus T for devices D1 (green open circles) and D2 (purple solid triangles). The red solid circles and blue open circles are, respectively, the contributions of the $1/f$ component and the Lorentzian component to the measured noise for device D1.

device prepared on the SiO_2 substrate, D2. The noise on SiO_2 substrate devices is more than two orders of magnitude larger than that of D1 and matches previous reports of measured noise in MoS_2 by various groups [37,39]. Our work thus shows that encapsulation helps to significantly improve the signal-to-noise ratio.

V. DISCUSSION

A careful study of Fig. 9 provides clues to the origin of the observed noise in this system. The temperature dependence of the relative variance of conductance fluctuations $\mathcal{G}_{\rm var}(T)$ measured for the on-SiO_2 substrate device D2 closely resembles the T dependence of the $1/f$ component of $\mathcal{G}_{\rm var}$ measured on D1. This indicates that these two noises have similar origins. The primary source of the T dependence of noise in many semiconductor devices is generation-recombination noise due to trapping and detrapping of charges at the gate dielectric-channel interfaces. This process can be quantified by the McWhorter model [40,60,61]:

$$N_{im} = f S_I(f) \langle R \rangle^2 \frac{WLC^2}{e^2 k_B} \frac{1}{T}, \tag{4}$$

where N_{im} is the areal density of trapped charges per unit energy, W and L are, respectively, the width and the length of the device channel, C is the gate capacitance per unit area, k_B is the Boltzmann constant, and e is the charge of the electron. Equation (4) predicts the linear dependence of $fS_I(f)$ on the temperature. Figure 10 shows a plot of $fS_I(f)$ versus T for both D1 and D2. The plots are linear to within experimental uncertainties. From the slopes of these plots, the value of N_{im} for device D2 was extracted to be $3.5 \times 10^{12}\ {\rm cm}^{-2}\ {\rm eV}^{-1}$, which agrees with previously reported values for MoS_2 devices prepared on SiO_2 substrates [62]. On the other hand, for the HfO_2-covered, on-hBN device

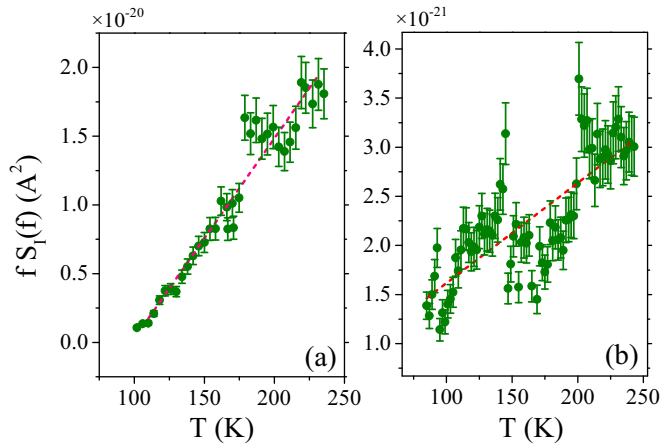

FIG. 10. Plot of $fS_I(f)$ versus T for the (a) on-SiO_2 substrate device D2 and (b) on-hBN HfO_2-encapsulated device D1. The red dashed lines in both plots are fits to Eq. (4).

D1, $N_{im} = 1.8 \times 10^{10}\ {\rm cm}^{-2}\ {\rm eV}^{-1}$, more than two orders of magnitude lower than that in the on-SiO_2 substrate device D2.

The non-$1/f$ seen only in the encapsulated device has a different origin. The presence of RTN in the time series of conductance fluctuations and the associated Lorentzian component in the PSD indicates that the noise originates from random charge fluctuations via transitions between two well-defined energy states separated by an energy barrier. We propose that in this case, these two levels correspond to the S-vacancy impurity band and the conduction band. This is supported by the fact that the value of the activation energy, $E_a = 370\,{\rm meV}$, extracted from the temperature dependence of the corner frequency f_C of the Lorentzian component of the current fluctuations matches closely with the estimated position of the S-vacancy impurity band with respect to the conduction-band edge [63]. Note that it was possible for us to detect this fluctuation component only because of the two

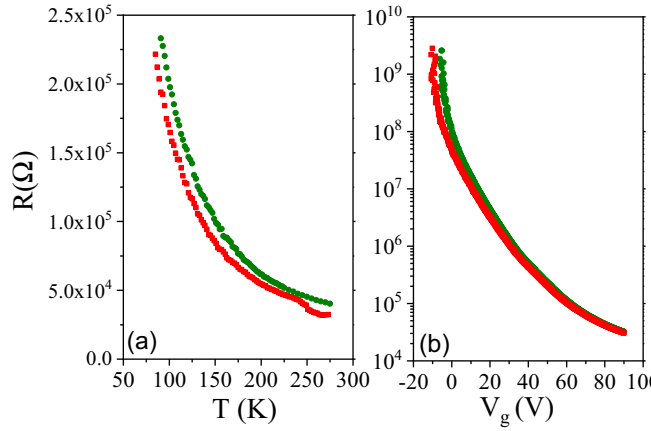

FIG. 11. (a) Comparison between the R versus T data at $V_g = 90\,{\rm V}$ for device D1 right after fabrication (red data points) and several months as well as several thermal cycles later (green data points). (b) Similar comparison of R versus V_g data measured at $T = 270\,{\rm K}$ for D1 in the pristine state and several months (and thermal cycles) later.

orders of noise reduction made possible by the introduction of hBN between the MoS_2 and SiO_2 substrate.

The HfO_2 layer has a twofold effect on the noise. First, being a high-k dielectric with a dielectric constant value of about 25, its presence screens the device from Coulomb scattering and reduces the $1/f$ noise by orders of magnitude, enabling us to detect the RTN. Second, it acts as a capping layer that shields the MoS_2 from the ambient. We believe that this prevents the S vacancies from getting saturated by adsorbates, thus preserving the RTN. With the current data, we cannot distinguish between these two effects. Preliminary results obtained on devices fabricated on hBN without the HfO_2 capping layer had higher on-off ratios, higher mobilities, and lower noise levels compared to MoS_2 devices fabricated on SiO_2 without the HfO_2 capping layer; however, we did not find any RTN in these devices. From these results, one can tentatively conclude that both the top and bottom layers are necessary to preserve the RTN. This issue is currently under detailed investigation.

Finally, coming to the question of stability of the devices, we have compared the R versus T, R versus V_g, and noise measurements on device D1 immediately after fabrication and after a gap of several months. The sample was thermally cycled several times during this period between 300 and 77 K. As shown in Fig. 11, the temperature and V_g dependence of the resistance of the device were quite reproducible. This is in sharp contrast to unencapsulated on-SiO_2 devices like D2, in which after a few days the channel and contacts both degrade drastically, making further measurements impossible [39]. Similarly, thermal cycling alters the characteristics of such devices and makes the channel resistance unstable. The stability of the resistance of D1 over a time period of months confirms that encapsulation between hBN and HfO_2 makes the device robust to thermal cycling and against degradation with time.

VI. CONCLUSION

To conclude, in this paper we reported on detailed conductance fluctuation spectroscopy of high-quality MoS_2 devices encapsulated between hBN and HfO_2. The presence of the high-κ dielectric made the device extremely stable against environmental degradation, enabling us to obtain reproducible data on the same device for over 1 year. The hBN substrate helped bring down the conductance fluctuations by over two orders of magnitude compared to similar devices on bare SiO_2 substrates. The low noise levels in our devices made it possible to detect the generation-recombination noise arising from charge fluctuation between the S-vacancy levels in the MoS_2 band gap and states at its conductance-band edge. Our work establishes conduction fluctuation spectroscopy as a viable route to detect in-gap defect levels in low-dimensional semiconductors.

ACKNOWLEDGMENTS

A.B. acknowledges funding from Nanomission and the FIST program, Department of Science & Technology (DST), government of India, and the Indo-French Centre for the Promotion of Advanced Research (CEFIPRA; Project No. 5304-F).

[1] K. S. Novoselov, A. K. Geim, S. V. Morozov, D. Jiang, Y. Zhang, S. V. Dubonos, I. V. Grigorieva, and A. A. Firsov, Science **306**, 666 (2004).
[2] K. F. Mak, C. Lee, J. Hone, J. Shan, and T. F. Heinz, Phys. Rev. Lett. **105**, 136805 (2010).
[3] Q. H. Wang, K. Kalantar-Zadeh, A. Kis, J. N. Coleman, and M. S. Strano, Nat. Nanotechnol. **7**, 699 (2012).
[4] H. Li, J. Wu, Z. Yin, and H. Zhang, Acc. Chem. Res. **47**, 1067 (2014).
[5] G. Eda and S. A. Maier, Acs Nano **7**, 5660 (2013).
[6] B. Radisavljevic, A. Radenovic, J. Brivio, I. V. Giacometti, and A. Kis, Nat. Nanotechnol. **6**, 147 (2011).
[7] J. Hong, Z. Hu, M. Probert, K. Li, D. Lv, X. Yang, L. Gu, N. Mao, Q. Feng, L. Xie *et al.*, Nat. Commun. **6**, 6293 (2015).
[8] Z.-Y. Ong and M. V. Fischetti, Phys. Rev. B **88**, 165316 (2013).
[9] H. Qiu, T. Xu, Z. Wang, W. Ren, H. Nan, Z. Ni, Q. Chen, S. Yuan, F. Miao, F. Song *et al.*, Nat. Commun. **4**, 2642 (2013).
[10] W. Zhu, T. Low, Y.-H. Lee, H. Wang, D. B. Farmer, J. Kong, F. Xia, and P. Avouris, Nat. Commun. **5**, 3087 (2014).
[11] S. McDonnell, R. Addou, C. Buie, R. M. Wallace, and C. L. Hinkle, ACS Nano **8**, 2880 (2014).
[12] S. Tongay, J. Suh, C. Ataca, W. Fan, A. Luce, J. S. Kang, J. Liu, C. Ko, R. Raghunathanan, J. Zhou *et al.*, Sci. Rep. **3**, 2657 (2013).
[13] N. Saigal and S. Ghosh, Appl. Phys. Lett. **109**, 122105 (2016).
[14] Y.-C. Lin, D. O. Dumcenco, H.-P. Komsa, Y. Niimi, A. V. Krasheninnikov, Y.-S. Huang, and K. Suenaga, Adv. Mater. **26**, 2857 (2014).
[15] X. Zou, Y. Liu, and B. I. Yakobson, Nano Lett. **13**, 253 (2012).
[16] A. M. Van Der Zande, P. Y. Huang, D. A. Chenet, T. C. Berkelbach, Y. You, G.-H. Lee, T. F. Heinz, D. R. Reichman, D. A. Muller, and J. C. Hone, Nat. Mater. **12**, 554 (2013).
[17] S. Najmaei, Z. Liu, W. Zhou, X. Zou, G. Shi, S. Lei, B. I. Yakobson, J.-C. Idrobo, P. M. Ajayan, and J. Lou, Nat. Mater. **12**, 754 (2013).
[18] S. Hosoki, S. Hosaka, and T. Hasegawa, Appl. Surf. Sci. **60-61**, 643 (1992).
[19] H. Permana, S. Lee, and K. S. Ng, J. Vac. Sci. Technol. B **10**, 2297 (1992).
[20] J. S. Ha, H.-S. Roh, S.-J. Park, J.-Y. Yi, and E.-H. Lee, Surf. Sci. **315**, 62 (1994).
[21] H. Murata, K. Kataoka, and A. Koma, Surf. Sci. **478**, 131 (2001).
[22] N. Kodama, T. Hasegawa, Y. Okawa, T. Tsuruoka, C. Joachim, and M. Aono, Jpn. J. Appl. Phys. **49**, 08LB01 (2010).
[23] R. Addou, L. Colombo, and R. M. Wallace, ACS Appl. Mater. Interfaces **7**, 11921 (2015).
[24] H.-P. Komsa, J. Kotakoski, S. Kurasch, O. Lehtinen, U. Kaiser, and A. V. Krasheninnikov, Phys. Rev. Lett. **109**, 035503 (2012).
[25] H.-P. Komsa, S. Kurasch, O. Lehtinen, U. Kaiser, and A. V. Krasheninnikov, Phys. Rev. B **88**, 035301 (2013).

[26] C.-P. Lu, G. Li, J. Mao, L.-M. Wang, and E. Y. Andrei, Nano Lett. **14**, 4628 (2014).
[27] Y. L. Huang, Y. Chen, W. Zhang, S. Y. Quek, C.-H. Chen, L.-J. Li, W.-T. Hsu, W.-H. Chang, Y. J. Zheng, W. Chen *et al.*, Nat. Commun. **6**, 6298 (2015).
[28] P. Vancsó, G. Z. Magda, J. Pető, J.-Y. Noh, Y.-S. Kim, C. Hwang, L. P. Biró, and L. Tapasztó, Sci. Rep. **6**, 29726 (2016).
[29] S. KC, R. C. Longo, R. Addou, R. M. Wallace, and K. Cho, Nanotechnology **25**, 375703 (2014).
[30] M. H. Naik and M. Jain, Phys. Rev. Mater. **2**, 084002 (2018).
[31] A. V. Krivosheeva, V. L. Shaposhnikov, V. E. Borisenko, J.-L. Lazzari, C. Waileong, J. Gusakova, and B. K. Tay, J. Semicond. **36**, 122002 (2015).
[32] Z. Lin, B. R. Carvalho, E. Kahn, R. Lv, R. Rao, H. Terrones, M. A. Pimenta, and M. Terrones, 2D Mater. **3**, 022002 (2016).
[33] J.-Y. Noh, H. Kim, and Y.-S. Kim, Phys. Rev. B **89**, 205417 (2014).
[34] P. Dutta and P. M. Horn, Rev. Mod. Phys. **53**, 497 (1981).
[35] S. H. Song, M.-K. Joo, M. Neumann, H. Kim, and Y. H. Lee, Nat. Commun. **8**, 2121 (2017).
[36] H.-J. Kwon, H. Kang, J. Jang, S. Kim, and C. P. Grigoropoulos, Appl. Phys. Lett. **104**, 083110 (2014).
[37] V. K. Sangwan, H. N. Arnold, D. Jariwala, T. J. Marks, L. J. Lauhon, and M. C. Hersam, Nano Lett. **13**, 4351 (2013).
[38] S. Ghatak, S. Mukherjee, M. Jain, D. D. Sarma, and A. Ghosh, APL Mater. **2**, 092515 (2014).
[39] J. Renteria, R. Samnakay, S. Rumyantsev, C. Jiang, P. Goli, M. Shur, and A. Balandin, Appl. Phys. Lett. **104**, 153104 (2014).
[40] J. Na, M.-K. Joo, M. Shin, J. Huh, J.-S. Kim, M. Piao, J.-E. Jin, H.-K. Jang, H. J. Choi, J. H. Shim *et al.*, Nanoscale **6**, 433 (2014).
[41] H. Qiu, L. Pan, Z. Yao, J. Li, Y. Shi, and X. Wang, Appl. Phys. Lett. **100**, 123104 (2012).
[42] D. J. Late, B. Liu, H. S. S. R. Matte, V. P. Dravid, and C. N. R. Rao, ACS Nano **6**, 5635 (2012).
[43] P. J. Kooyman and J. R. van Veen, Catal. Today **130**, 135 (2008).
[44] C. R. Dean, A. F. Young, I. Meric, C. Lee, L. Wang, S. Sorgenfrei, K. Watanabe, T. Taniguchi, P. Kim, K. L. Shepard *et al.*, Nat. Nanotechnol. **5**, 722 (2010).
[45] K. L. Ganapathi, N. Bhat, and S. Mohan, Appl. Phys. Lett. **103**, 073105 (2013).
[46] K. L. Ganapathi, N. Bhat, and S. Mohan, Semicond. Sci. Technol. **29**, 055007 (2014).
[47] S. Kim, A. Konar, W.-S. Hwang, J. H. Lee, J. Lee, J. Yang, C. Jung, H. Kim, J.-B. Yoo, J.-Y. Choi *et al.*, Nat. Commun. **3**, 1011 (2012).
[48] V. K. Sangwan and M. C. Hersam, Annu. Rev. Phys. Chem. **69**, 299 (2018).
[49] J. Mao, J. Shuai, S. Song, Y. Wu, R. Dally, J. Zhou, Z. Liu, J. Sun, Q. Zhang, C. dela Cruz *et al.*, Proc. Natl. Acad. Sci. USA **114**, 10548 (2017).
[50] C. Liu, K. Huang, W.-T. Park, M. Li, T. Yang, X. Liu, L. Liang, T. Minari, and Y.-Y. Noh, Mater. Horiz. **4**, 608 (2017).
[51] A. Bid, Resistance fluctuations and instability in metal nanowires. Ph.D. thesis, Indian Institute of Science, 2006.
[52] G. N. Daptary, P. Kumar, A. Dogra, and A. Bid, Phys. Rev. B **98**, 035433 (2018).
[53] P. Price, Ann. Phys. (NY) **133**, 217 (1981).
[54] F. Hooge, IEEE Trans. Electron Devices **41**, 1926 (1994).
[55] J. H. Scofield, Rev. Sci. Instrum. **58**, 985 (1987).
[56] F. K. Du Pré, Phys. Rev. **78**, 615 (1950).
[57] H. K. Kundu, S. Ray, K. Dolui, V. Bagwe, P. R. Choudhury, S. B. Krupanidhi, T. Das, P. Raychaudhuri, and A. Bid, Phys. Rev. Lett. **119**, 226802 (2017).
[58] K. K. Hung, P. K. Ko, C. Hu, and Y. C. Cheng, IEEE Electron Device Lett. **11**, 90 (1990).
[59] F. Hooge, T. Kleinpenning, and L. Vandamme, Rep. Prog. Phys. **44**, 479 (1981).
[60] A. H. McWhorter, *Semiconductor Surface Physics* (University of Pennsylvania Press, Philadelphia, 1957), p. 207.
[61] G. Ghibaudo, O. Roux, C. Nguyen-Duc, F. Balestra, and J. Brini, Phys. Status Solidi A **124**, 571 (1991).
[62] S. Dubey, S. Lisi, G. Nayak, F. Herziger, V.-D. Nguyen, T. Le Quang, V. Cherkez, C. González, Y. J. Dappe, K. Watanabe *et al.*, ACS Nano **11**, 11206 (2017).
[63] M. Ghorbani-Asl, A. N. Enyashin, A. Kuc, G. Seifert, and T. Heine, Phys. Rev. B **88**, 245440 (2013).